

Article

Revisiting a Quasar Microlensing Event Towards AGN J1249+3449

Mario Cazzolla ¹, Francesco De Paolis ^{1,2,3*}, Antonio Franco ^{1,2,3} and Achille Nucita ^{1,2,3}

¹ Department of Mathematics and Physics “E. De Giorgi”, University of Salento, Via per Arnesano, CP-I93, I-73100 Lecce, Italy; mario.cazzolla@studenti.unisalento.it (M.C.); antonio.franco@le.infn.it (A.F.); achille.nucita@le.infn.it (A.N.)

² INFN (Istituto Nazionale di Fisica Nucleare), Sezione di Lecce, Via per Arnesano, CP-193, I-73100 Lecce, Italy

³ INAF (Istituto Nazionale di Astrofisica), Sezione di Lecce, Via per Arnesano, CP-193, I-73100 Lecce, Italy

* Correspondence: francesco.depaolis@le.infn.it

Abstract

The gravitational wave event GW190521 seems to be the only BH merger event possibly correlated with an electromagnetic counterpart, which appeared about 34 days after the GW event. This work aims to confirm that the electromagnetic bump towards the Active Galactic Nucleus (AGN) J1249+3449 can be explained within the framework of the gravitational microlensing phenomenon. In particular, considering the data of the Zwicky Transient Facility (ZTF), what emerges from a detailed analysis of the observed light curve using three fitting models (Point Source Point Lens, Finite Source Point Lens, Uniform Source Binary Lens) is that the optical bump can be explained as a microlensing event caused by a lens with mass $\sim 0.1 M_{\odot}$, lying in the host galaxy of the AGN in question.

Keywords: gravitational waves; gravitational lensing: micro; quasars: individual: AGN J1249+3449; time series analysis; computational astronomy; astronomy data modeling

1. Introduction

On 21 May 2019, at 03:02:29 UTC, the LIGO [1] and VIRGO [2] interferometers revealed a gravitational wave (GW) event, named GW190521, from a candidate binary black hole (BBH) merger towards AGN J1249+3449, with a false alarm rate of 3.8×10^{-9} Hz [3]. The performed analysis allowed constraints on the physical parameters of the system [3,4], as follows:

$$\left\{ \begin{array}{l} M_1 = 85_{-14}^{+21} M_{\odot}, \\ M_2 = 66_{-18}^{+17} M_{\odot}, \\ M_{res} = 142_{-16}^{+28} M_{\odot}, \\ D_l = 3931 \pm 953 \text{ Mpc}, \end{array} \right. \quad (1)$$

where M_1 and M_2 represent the masses of the black holes which took part in the merging event, M_{res} is the resulting mass after the black holes coalesce, and D_l is the luminosity distance of the system. In [4] the latter quantity is quantified as $5.3_{-2.6}^{+2.4}$ Gpc, but, for the whole article, the value estimated in [3] has been taken into consideration.

Approximately 34 days after the GW event, an electromagnetic flare was detected by the Zwicky Transient Facility (ZTF)¹ [6]. In [3], the authors associated this flare with a probable electromagnetic counterpart of the merger in the AGN disk, excluding other possible explanations such as intrinsic variability of the AGN, a supernova, a tidal disruption event or a microlensing event.

The latter scenario had been discarded because the expected characteristic timescale for microlensing is in the order of years, which is inconsistent with the several-week flare considered; furthermore, an event rate estimate was calculated: “assuming a M_{\odot} lens in the source galaxy, the lens is required to orbit at ~ 1 kpc with a transverse velocity of about 200 km/s in order to match the timescale ($\sim 2 \times 10^6$ s) and magnification (~ 1.4) of this event; assuming a population of $O(10^{10})$ stars in appropriate orbits, geometric considerations produce a rate of $O(10^{-5})$ events $\text{yr}^{-1} \text{AGN}^{-1}$ ” [3].

Just after the discovery of the electromagnetic flare, a discussion of its nature began in the astronomical community, since no electromagnetic counterpart is expected for black hole mergers. Indeed, in [7] it is shown that the detected optical light curve is well fitted by a microlensing event due to a lens with mass about $0.1 M_{\odot}$ lying in the AGN disk. The analysis allowed for constraining the system parameters, as follows:

$$\begin{cases} t_0 = 469 \pm 1 \text{ days}, \\ t_E = 17.6 \pm 1.2 \text{ days}, \\ u_0 = 0.92 \pm 0.03, \\ m_b = 19.082 \pm 0.003. \end{cases} \quad (2)$$

Here, t_0 is the time of closest approach between the lens and the source, and it is expressed considering $MJD = 58,202.293102$ (the start of data acquisition, expressed in Modified Julian Date) as $t = 0$. u_0 is the impact parameter in units of the Einstein radius, m_b is the magnitude of the source baseline (the intrinsic flux of the source, in the absence of the microlensing event), and t_E is the Einstein crossing time:

$$t_E = \frac{r_E}{v_{\perp}} = \frac{\theta_E D_L}{v_{\perp}}, \quad (3)$$

where v_{\perp} is the relative transverse velocity between the source and lens due to the proper motions of Earth, lens and source, r_E and θ_E are the physical and angular Einstein ring radius, respectively, and D_L is the distance to the lens.

As mentioned in [7], detecting such transient events is very challenging, so it is necessary to acquire a large amount of data to understand these events better. Therefore, the aim of this article is to study the AGN light curve coming from the AGN with more recent data (in order to show that, for the entire light curve, there are no periodic repetitions of the bump, which can be due to the activity of the quasar), since the above-mentioned articles [3,4,7] considered data until 2019. For this reason, in the present paper, a new set of data (the “data release 23” of the ZTF), with g , r , and i SDSS magnitudes, which covers a time interval going from March 2018 to October 2024, has been taken into consideration.

2. Event Modelization

Throughout the paper, the ZTF light curve is fitted by using three microlensing models, each with a different number of free parameters:

- Point Source Point Lens (PSPL, Section 2.1): fitted through the Levenberg–Marquardt (LM) algorithm, the Differential Evolution (DE) algorithm and the Markov Chain Monte Carlo (MCMC) method.
- Finite Source Point Lens (FSPL, Section 2.2): fitted through the Differential Evolution and the Markov Chain Monte Carlo method. The LM method is not applicable for this and for the next model because the function “LM_fit” of pyLIMA² is not compatible with them (for further details see [8]).
- Uniform Source Binary Lens (USBL, Section 2.3): fitted using the same algorithms as the FSPL model.

In the following, only the results obtained with the MCMC method will be illustrated, as this algorithm yields more precise outcomes. Indeed, the starting parameters are taken from the DE results, and the latter are taken from the LM method. The process of considering the previous results as the starting point for the next model has been followed since it allows for faster convergence of the fit. Moreover, the MCMC algorithm returns more realistic and stable estimations of the uncertainties than the other methods; however, this accuracy makes the MC algorithm about 2000 times slower with respect to the LM method, since it requires the computation of thousands of models [8].

2.1. PSPL Model

Since the non-negligible redshift of the source generates differences between the comoving distance, the luminosity distance and the angular distance, in this paragraph, the description made by Gould [9] will be followed using the angular distances (see [10]). In microlensing events, the lens object is, in general, a star nearly crossing the line of sight between the observer and a background source. Inverting the standard microlensing geometry, i.e., projecting the Einstein ring onto the observer plane rather than the source plane, an evident relation arises between the observable θ_E and \tilde{r}_E , the projected Einstein radius, and the physical quantities M_L and π_{rel} , the lens mass and the lens–source relative parallax, respectively (see Figure 1).

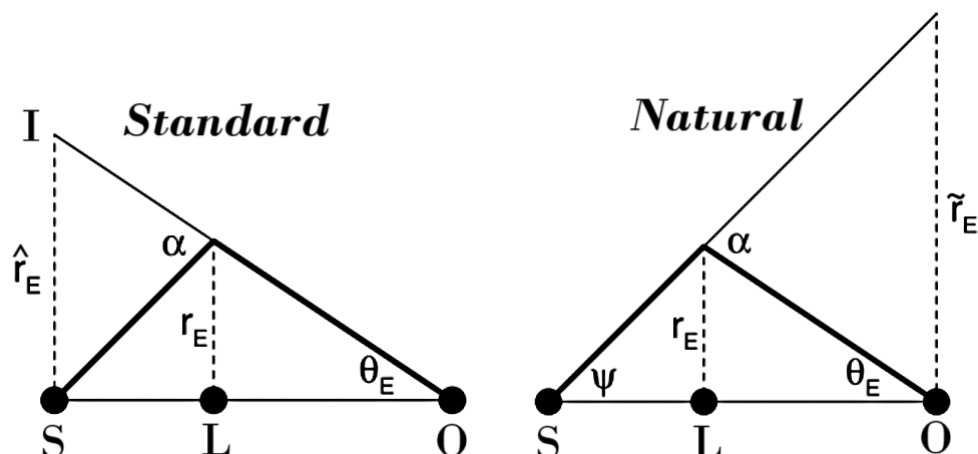


Figure 1. (Left Panel): standard microlensing geometry; the bold curve shows the path of the light from the source (S) to the observer (O) being deflected by the lens (L) of mass M_L . The image (I) is displaced from the source by the angular Einstein radius θ_E , which, projected onto the source plane, corresponds to a physical distance \hat{r}_E . **(Right Panel):** natural microlensing geometry; mostly the same as the left panel except that the Einstein radius is now projected onto the observer plane as \tilde{r}_E rather than onto the source plane as \hat{r}_E . Figure adapted from [9].

In the new geometry, using the small-angle approximation ($\tan \theta \approx \sin \theta \approx \theta$), one can note that

$$\frac{\alpha}{\tilde{r}_E} = \frac{\theta_E}{r_E} \iff \theta_E \tilde{r}_E = \alpha r_E = \frac{4GM_L}{c^2}. \quad (4)$$

Next,

$$\theta_E = \alpha - \psi = \frac{\tilde{r}_E}{D_L} - \frac{\tilde{r}_E}{D_S} = \frac{\tilde{r}_E}{D_{rel}}, \quad (5)$$

in which D_S is the distance to the source and $D_{rel}^{-1} \equiv D_L^{-1} - D_S^{-1}$. The equation for the angular Einstein radius can be rewritten as

$$\pi_E \theta_E = \pi_{rel}, \quad \pi_E \equiv \frac{AU}{\tilde{r}_E}, \quad (6)$$

where $\pi_{rel} \equiv \frac{AU}{D_{rel}}$ is the lens–source relative parallax, and $1 AU \equiv 1.496 \times 10^8$ km indicates the astronomical unit.

From these equations, one gets

$$\tilde{r}_E = \sqrt{\frac{4GM_L D_{rel}}{c^2}}, \quad \pi_E = \sqrt{\frac{\pi_{rel}}{\kappa M_L}}, \quad \theta_E = \sqrt{\frac{4GM_L}{c^2 D_{rel}}} = \sqrt{\kappa M_L \pi_{rel}}, \quad (7)$$

where $\kappa \equiv \frac{4G}{AUc^2} \simeq 8.144 \frac{mas}{M_\odot}$. The standard parametrization in terms of the microlensing parallax vector components takes into account the East and North components, i.e., π_{EE} and π_{EN} respectively, whose composition gives the π_E vector absolute value:

$$\pi_E = \sqrt{\pi_{EE}^2 + \pi_{EN}^2}. \quad (8)$$

Combining the first expression of Equation (6) and the last of Equation (7), it is possible to obtain an equation for the lens mass:

$$M_L = \frac{\theta_E}{\kappa \pi_E}. \quad (9)$$

Each image is magnified and the source flux increases by the total magnification factor $\mu(t)$, which, for the PSPL model, is given by Paczyński [11]:

$$\mu_{PSPL} = \frac{u(t)^2 + 2}{u(t)\sqrt{u(t)^2 + 4}}, \quad u(t) = \sqrt{u_0^2 + \frac{(t - t_0)^2}{t_E^2}}, \quad (10)$$

where $u(t)$ is the source–lens impact parameter and $u_0 = u(t_0)$ is the minimum impact parameter at the time t_0 .

2.2. FSPL Model

In the PSPL model, it is assumed that the source is a point-like object. However, this hypothesis breaks down when the source-lens separation becomes small enough to be comparable to (or not negligible with respect to) the normalized angular source radius $\rho = \frac{\theta_S}{\theta_E}$, where θ_S is the angular radius of the source. “This indicates that finite source effects often appear in the case of highly magnified events” [8]. In the scenario of an extended source, assuming that it emits homogeneously up to the angular radius ρ , the total amplification is calculated by integrating the amplification μ_{tot} over the source area S [12]:

$$\mu^*(u, \rho) = \frac{\int_S \mu(t) dS}{\int_S dS} = \frac{1}{\pi \rho^2} \int_S \mu(t) dS, \quad (11)$$

in which $\mu(t)$ is given by the PSPL model in Equation (10).

Since ρ is defined as the source size in units of the Einstein angle, estimating the ρ value makes it easier to estimate the Einstein angle through the relation:

$$\theta_E = \frac{R_S}{\rho D_S}, \quad (12)$$

where R_S is the source radius.

2.3. USBL Model

A binary lens consists of a two-mass system, composed of two objects with masses M_1 and M_2 . The lens plane coordinate system (x, y) is arranged so that the x -axis passes through the projection of the masses onto the lens plane, with the origin at the central point

between the two lens masses (Figure 2). Each member of the binary system is considered to be at a distance D_L from the observer, with their separation being relatively small.

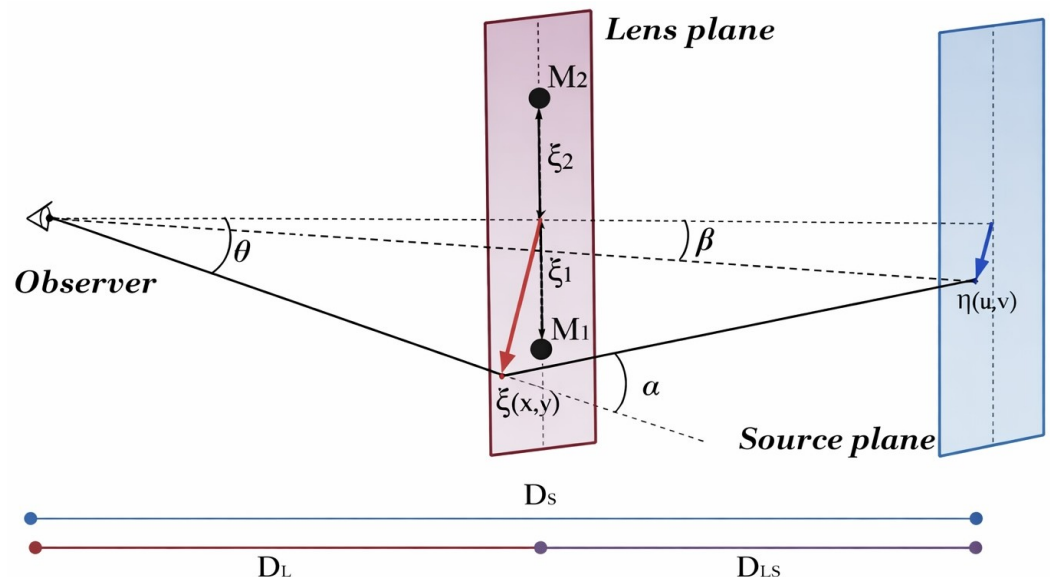


Figure 2. The geometry of a binary lens system. The lens plane is defined by the coordinate system (x, y) , with the x -axis passing through the projection of the two masses onto the plane itself, with the central point between the lens objects. The source plane is, instead, expressed by the coordinate system (u, v) , presenting its origin at the intersection point between the plane and the optical axis. ξ_1 and ξ_2 are the vector positions of the projection points of the masses (M_1 and M_2) in the lens plane geometry; α represents the deflection angle, β indicates the angular position of the point $\eta(u, v)$ in the source plane in which the light ray originates, and θ is the angular position of the intersection point $\xi(x, y)$ between the light ray and the lens plane. The distances are expressed as follows: D_L is the distance between the observer and the lenses, D_{LS} stands for the distance between the binary lens and the source, and D_S indicates the distance between the observer and the source. Figure adapted from [13].

The source plane is described by the coordinate system (u, v) , with its origin at the point where the optical axis intersects the plane. Each mass deflects a light ray from the source by the angle $\alpha = \frac{4GM_L}{c^2 b}$ [14,15], where G is the Gravitational Constant and b is the impact parameter between the photon and the lens mass. Consequently, the total deflection is then the vector sum of the deflections by each of the individual masses.

For this study, the light curve of a microlensing event due to a binary lens system can be modeled using seven parameters: the mass ratio q , the binary separation s , the time t_0 of the projected closest separation between the source and the binary center of mass, the Einstein time t_E , the impact parameter u_0 with respect to the center of mass, the source finite size R_S , and the source trajectory angle γ with respect to the binary lens axis. The light curve for a generic binary lens system derives from the solution of the lens equation, which, in complex notation, can be written as follows [16–18]:

$$\eta = \xi + \frac{M_1}{\xi_1 + \bar{\xi}} + \frac{M_2}{\xi_2 + \bar{\xi}} \quad (13)$$

where $\eta = u + iv$ and $\xi = x + iy$ are the positions of the source and image, respectively, and ξ_1 and ξ_2 are the positions of the two lenses. The shape of the light curve depends on the binary separation or, more precisely, on the projected separation into the sky distance between the two components at the time of interest, expressed in Einstein radius units, $s = \frac{a_{\perp}}{D_L \theta_E}$, where a_{\perp} represents the projected physical separation between the lens masses expressed in AU.

3. Light Curve Analysis

A microlensing event fulfills the following properties:

- The observed light curve is achromatic since the gravitational bending of light is independent of the frequency of the radiation (even though the size and position of the source could shift a bit between the different energies, causing effects that depend on the wavelength).
- For a single lens event, the observed bump should be symmetric with respect to its maximum, and the overall shape depends on four parameters: the Einstein crossing times t_E , the impact parameter u_0 , the time of closest approach t_0 and the magnitude of the source baseline m_b .
- Outside the microlensing event, the source is characterized by a constant flux, and the light curve does not present any periodic feature, unless in the case of a binary source or a binary lens with orbital time much less than the microlensing event duration (for details see, e.g., [19,20]).

In Figure 3, the $g - r$ color for the AGN J1249+3449 light curve is shown (the i band has not been considered due to the small number of data points). Through the interpolation, it is possible to associate a common baseline for the r and g band data, since they have, a priori, different baselines. As one can see, the overall behavior of the $g - r$ light curve is almost achromatic (constant with time), giving further support to the microlensing nature of the considered event.

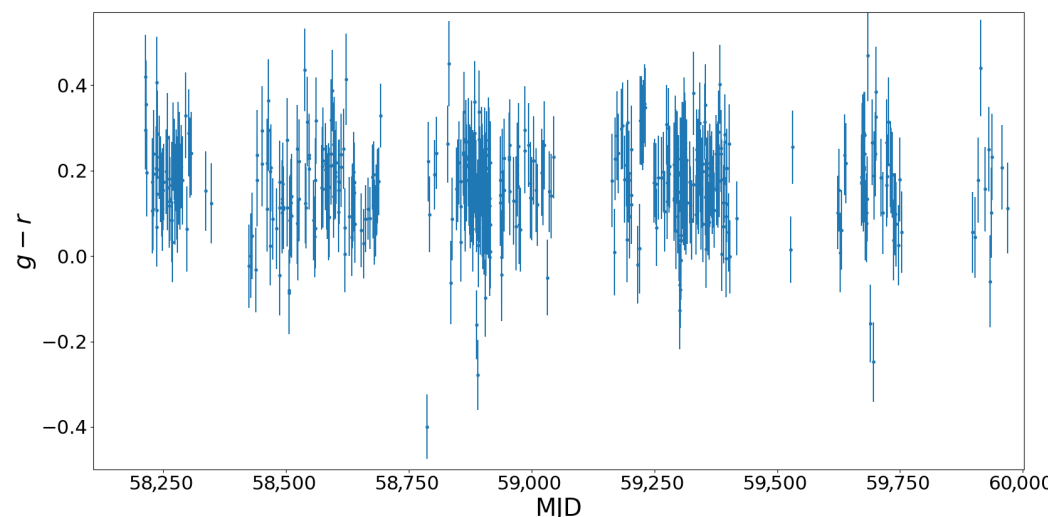


Figure 3. The $g - r$ color for the AGN J1249+3449 light curve is shown on the vertical axis, while the horizontal axis represents the time expressed in MJD. For this figure, the r band magnitudes have been interpolated at the time of the g band measurements. The range of time ends at approximately 60,000 since it includes the whole microlensing event and does not consider the last group of points, where the concentration of r band data is very low. The magnitude remains constant for the entire graph.

4. Results

As mentioned above, the light curve was fitted with three different models (six if the parallax effect was included in each of them) through the use of the open-source software pyLIMA [8]: the first couple considered was that formed by the PSPL model and the PSPL + parallax model; subsequently, more realistic and complex models, i.e., the FSPL model and the FSPL + parallax model, were taken into consideration; the last situation treated was that of an event caused by a binary lens, through the inclusion of the USBL and USBL + parallax models.

Tables 1–3 show the models' parameters and their corresponding values, obtained using the MCMC fitting algorithm.

Table 1. Parameters of the adopted models with their units and a brief description.

Parameter	Unit	Description
t_0	days	Time of the minimum impact parameter
u_0	θ_E	Minimum impact parameter defined on the center of mass of the lens system (positive if the source passes on the left of the source)
t_E	days	Angular Einstein ring crossing time
ρ	θ_E	Normalized angular source radius
s	θ_E	Normalized angular separation between the binary lens component
q		Binary mass ratio
γ	rad	Angle between the source trajectory and the binary lens axis (anti-clockwise)
π_{EN}	AU/ r_E	North component of the microlensing parallax
π_{EE}	AU/ r_E	East component of the microlensing parallax

Table 2. Obtained values for the parameters in the case of non-parallax models. The given errors have been estimated by the MCMC fitting algorithm. The * symbol is used when a parameter is not included in the corresponding model.

	PSPL	FSPL	USBL
t_0	$58,670.64^{+0.93}_{-0.79}$	$58,670.91^{+1.00}_{-0.95}$	$59,084.1^{+4.1}_{-9.7}$
u_0	$0.17^{+0.58}_{-0.94}$	$0.44^{+0.36}_{-0.89}$	0.09 ± 0.01
t_E	$23.9^{+10.0}_{-4.3}$	$25.7^{+11.0}_{-5.5}$	$380.2^{+8.9}_{-17.0}$
ρ	*	0.03 ± 0.02	$0.26^{+1.80}_{-0.24} \times 10^{-3}$
s	*	*	2.51 ± 0.06
q	*	*	$0.98^{+0.02}_{-0.04}$
γ	*	*	3.09 ± 0.01
χ^2	2967.13	2967.14	2418.94
χ^2/dof	1.86	1.86	1.53

Table 3. Obtained values for the parameters in the case of parallax models. The given errors have been estimated by the MCMC fitting algorithm. The * symbol is used when a parameter is not included in the corresponding model.

	PSPL + Parallax	FSPL + Parallax	USBL + Parallax
t_0	$58,630^{+72}_{-41}$	$58,647^{+65}_{-93}$	$58,633^{+42}_{-30}$
u_0	$-0.05^{+0.72}_{-0.69}$	$0.15^{+0.66}_{-0.84}$	$0.06^{+0.55}_{-0.74}$
t_E	28^{+14}_{-8}	29^{+18}_{-10}	$21.9^{+3.8}_{-3.7}$
ρ	*	0.02 ± 0.02	$0.5^{+7.3}_{-0.4} \times 10^{-3}$
s	*	*	$0.65^{+1.05}_{-0.10}$
q	*	*	$0.29^{+0.18}_{-0.15}$
γ	*	*	$5.41^{+0.13}_{-0.14}$
π_{EN}	$0.08^{+0.11}_{-0.14}$	$-0.09^{+0.16}_{-0.10}$	0.07 ± 0.09
π_{EE}	$-0.23^{+0.41}_{-0.16}$	$-0.18^{+0.40}_{-0.26}$	$-0.36^{+0.37}_{-0.11}$
χ^2	2963.32	2958.23	6432.78
χ^2/dof	1.85	1.85	4.02

As can be seen from Table 3, for all the parallax models, the two components π_{EN} and π_{EE} are compatible with 0. This result is due to the fact that the event occurs over

tens of days, whereas a non-negligible parallax contribution is obtained in a few months. Furthermore, the USBL model presents the greatest χ^2 value since the data do not properly constrain it, resulting in an unrealistic model. For this reason, the analysis was conducted considering only non-parallax models.

In the case of the latter models, it was possible to calculate the Einstein angle θ_E using Equation (3), after accounting for the lens masses and separation (for the USBL model). Since the geometry of the event suggests the presence of the lens within the lens host galaxy [7], we chose a range of the lens–source distance D_{LS} between 5 kpc and 100 kpc. Indeed, it can be expected that the lens object is not too close to the center of the galaxy, occupied by a Supermassive Black Hole (SMBH) of $10^{8-9} M_\odot$, nor too far from it, since the distribution of celestial bodies (which eventually could generate a microlensing event) in the galaxy decreases with the distance from its center.

Then, assuming a transverse velocity $v_\perp = 300$ km/s, the lens mass is plotted as a function of D_{LS} (see Figure 4) for the three considered models.

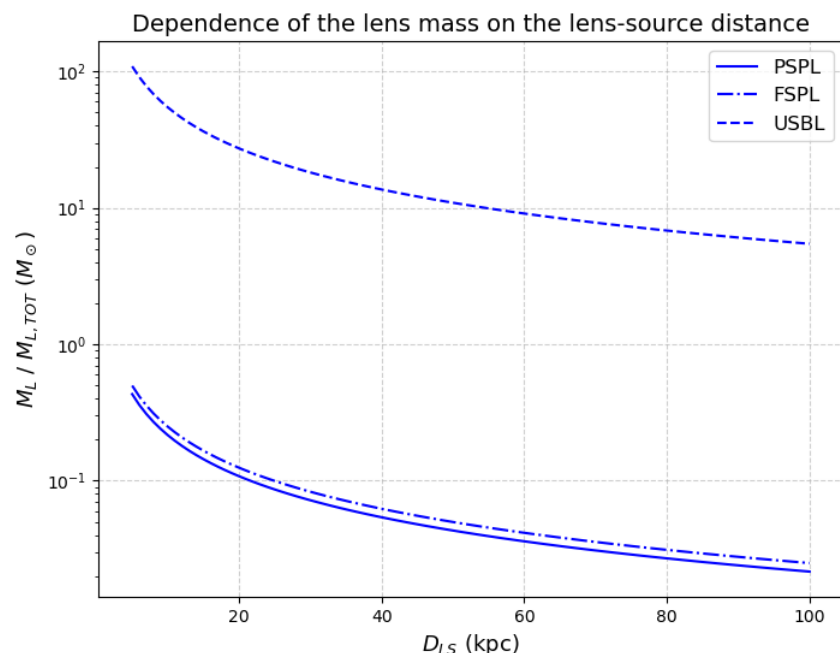


Figure 4. Dependence of the lens mass M_L in M_\odot (for PSPL and FSPL models) and of the total lens mass system $M_{L,TOT}$ in M_\odot (for the USBL model) with respect to the lens–source distance D_{LS} (in kpc). The y -axis, rescaled logarithmically, represents the lens mass, while the distance is graphed in the linear x -axis. These two parameters are linked by the equation for the calculation of the Einstein time of the event t_E (Equation (3)), which can be rewritten as follows (considering $D_L \simeq D_S$): $M_L = \frac{(t_E c v_\perp)^2}{4 G D_{LS}}$. The PSPL model is characterized by a continuous line, the FSPL model by a dash-dotted line, and the USBL model by a dashed line.

In order to present a realistic system and geometry of the event, a reasonable value of D_{LS} was chosen for the analysis; this value is related to the probability that the microlensing event can occur, thanks to the presence of celestial objects in the galaxy. The distance chosen was 20 kpc, and with it, the calculations of mass and separation (in the USBL model) were carried out. The values obtained are presented in Table 4.

As can be seen from Table 2, the introduction of the parameter ρ for the FSPL model does not involve a better estimation of the χ^2 ; furthermore, its value is not significant enough to make this model more convincing than the PSPL model.

Table 4. Best fit values of the lens masses and their relative separation a_{\perp} obtained by the PSPL, FSPL and USBL models, considering $D_{LS} = 20,000$ pc and $v_{\perp} = 300$ km/s. The * symbol is used when a parameter is not included in the corresponding model. The errors are calculated using the standard formula for the propagation of uncertainty of a function $f(x, y, \dots)$: $\sigma_f = \sqrt{\left|\frac{\partial f}{\partial x}\right|^2 \sigma_x^2 + \left|\frac{\partial f}{\partial y}\right|^2 \sigma_y^2 + \dots}$

	PSPL	FSPL	USBL
$M_{L1} (M_{\odot})$	0.10	0.12	13.2
$M_{L2} (M_{\odot})$	*	*	13.4
a_{\perp} (AU)	*	*	162 ± 57

Figure 5, showing the light curve fitted with the USBL model, is characterized by two additional bumps after the main event, which are not predicted in the PSPL and FSPL models (see Figures 6 and 7).

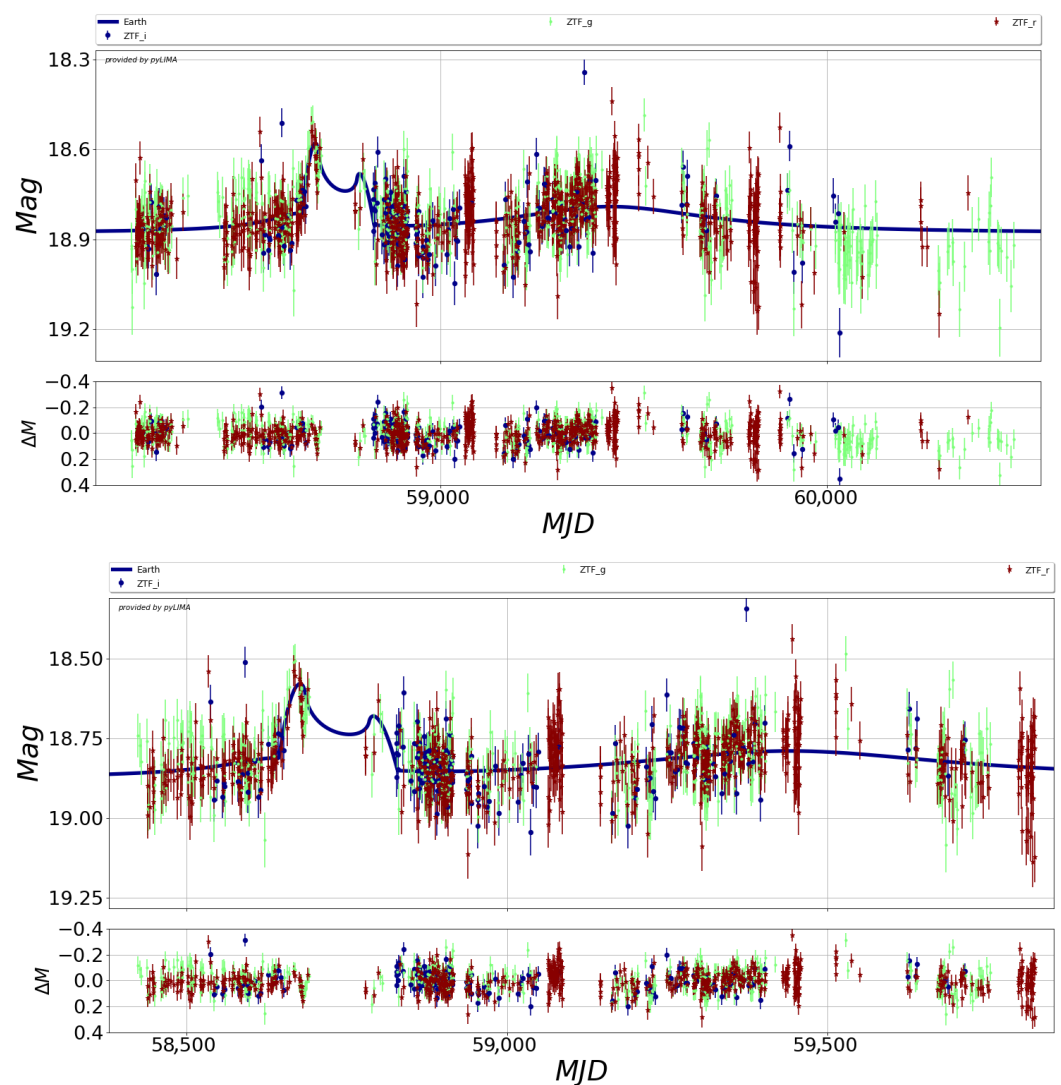


Figure 5. (Upper panel): Light curve of the AGN J1249+3449 fitted with the USBL model and the model residuals with respect to the best fit, with the vertical axis showing the magnitude of the source. **(Lower panel):** Close-up of the light curve and the model residuals, with the magnitude expressed on the vertical axis. For both panels, the horizontal axis represents the time expressed in MJD. The green points indicate the data in the *g* band, the red ones the data in the *r* band, and the blue points represent the data in the *i* band. All the magnitudes are intrinsically corrected, with respect to a common baseline, by pyLIMA.

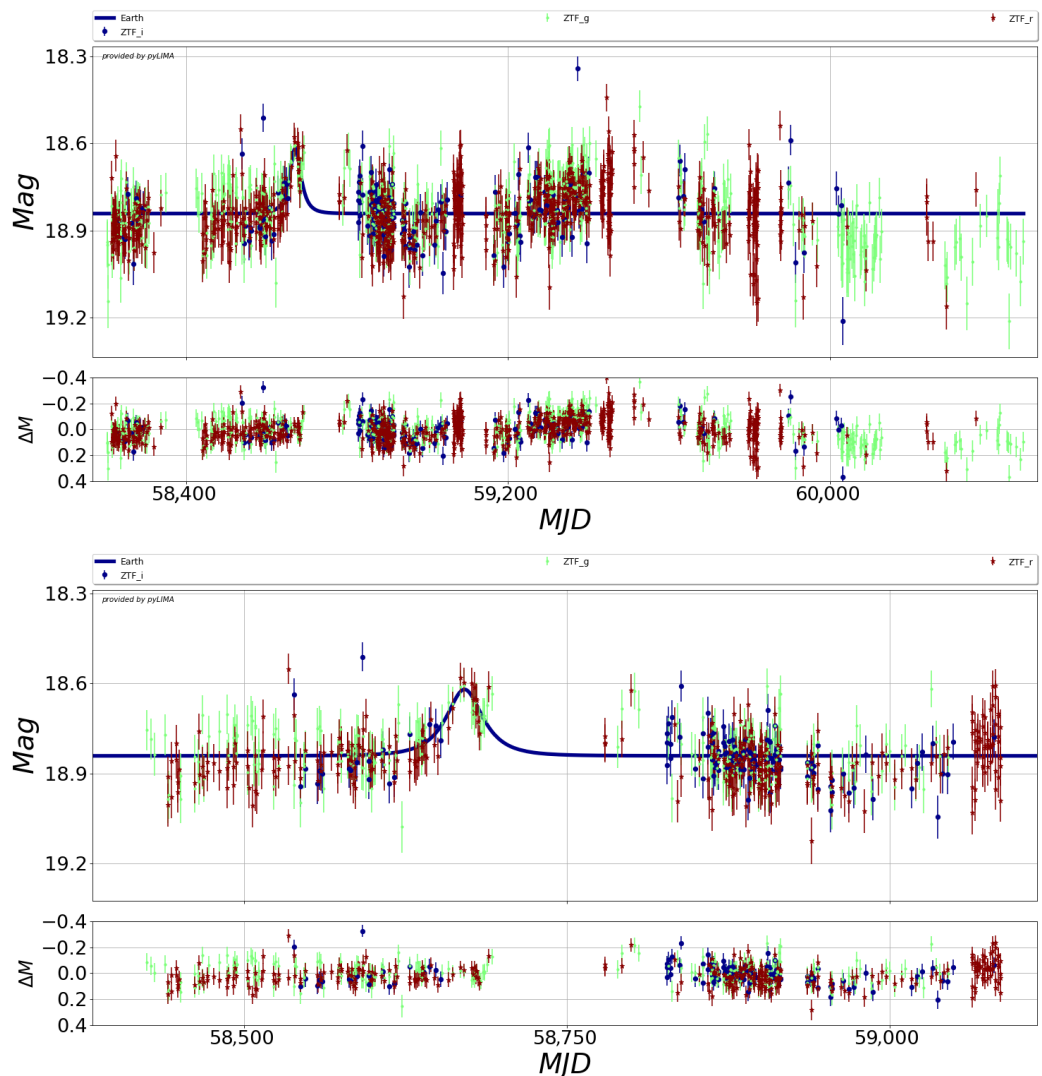


Figure 6. (Upper panel): Light curve of the AGN J1249+3449 fitted with the PSPL model and the model residuals with respect to the best fit, with the vertical axis showing the magnitude of the source. **(Lower panel):** Close-up of the light curve and the model residuals, with the magnitude expressed on the vertical axis. For both panels, the horizontal axis represents the time expressed in MJD. Colors follow the definition given in the caption of Figure 5. All the magnitudes are intrinsically corrected, with respect to a common baseline, by pyLIMA.

Even though the fit presents a smaller value of the χ^2 , the previous considerations, and the fact that the value of a_{\perp} does not belong to 1–100 AU, the typical separation interval of binary systems, allow us to conclude that the USBL model cannot properly account for the quasar light curve.

In conclusion, the previous discussion reveals that the PSPL model provides the best description of the light curve of AGN J1249+3449, and the most likely point-like lens mass turns out to be $\sim 0.1 M_{\odot}$.

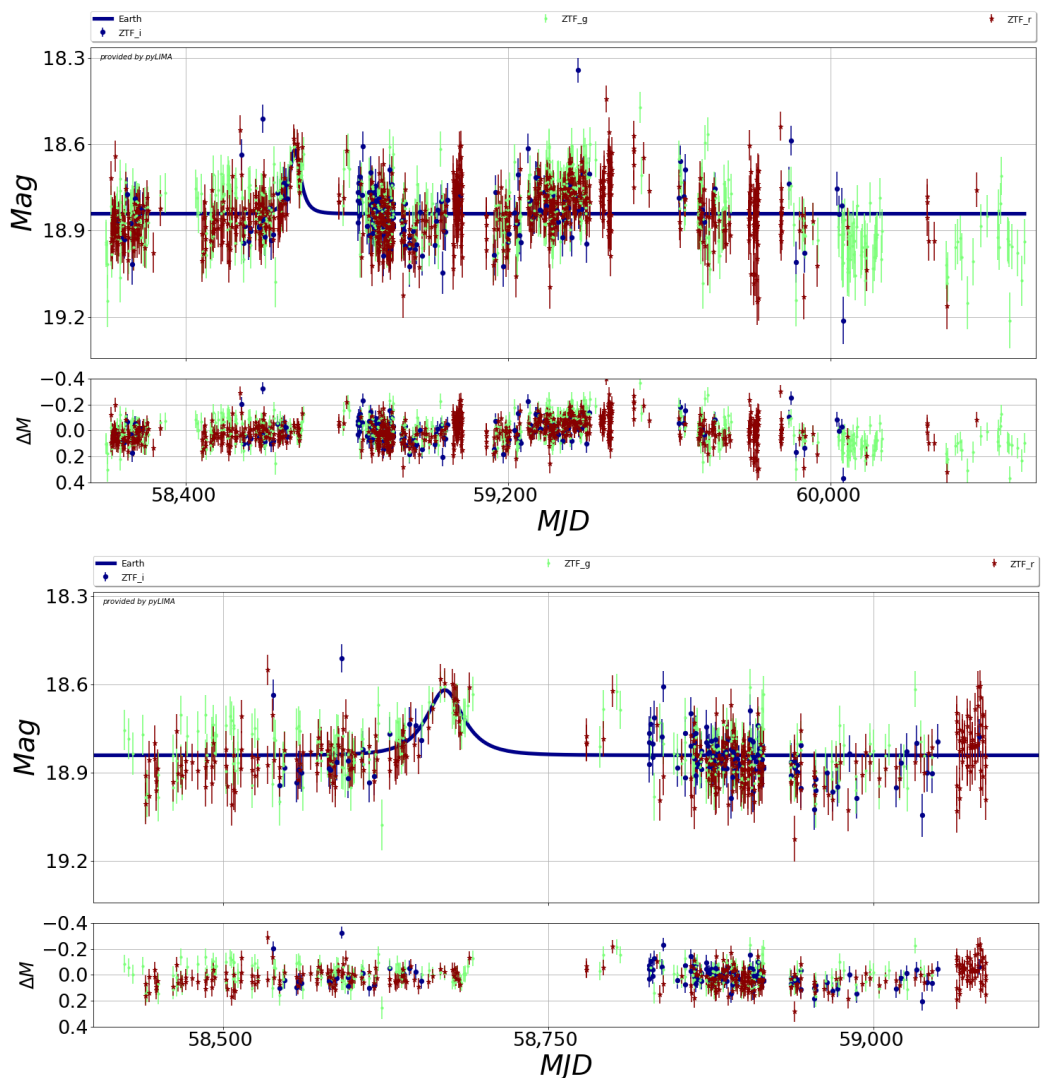


Figure 7. (Upper panel): Light curve of the AGN J1249+3449 fitted with the FSPL model and the model residuals with respect to the best fit, with the vertical axis showing the magnitude of the source. **(Lower Panel):** Close-up of the light curve and the model residuals, with the vertical axis representing the magnitude. For both panels, the horizontal axis represents the time expressed in MJD. Colors follow the definition given in the caption of Figure 5. All the magnitudes are intrinsically corrected, with respect to a common baseline, by pyLIMA.

5. Conclusions

The first studies of the flare event towards AGN J1249+3449 were conducted by Graham and colleagues [3], who reported the discovery of a flare-like structure in the quasar's light curve, affirming that this could be the sign of an optical electromagnetic counterpart to a binary black hole merger event. In the same year, the research group led by De Paolis reanalyzed the light curve and found that the flare-like signal could be associated with a microlensing event (see [7]).

In the present paper, the light curve is examined using significantly more data than in the previous analyses. What emerges is a confirmation of the microlensing hypothesis. Indeed, the light curve is fitted with various microlensing models (the PSPL model, the FSPL model and the USBL model), showing that the event respects the three minimal requirements for claiming the microlensing nature (see Section 3). The most convincing model is the PSPL model, which returns a lens with a mass of $\sim 0.1 M_{\odot}$, in agreement with the value previously found in [7].

With $0.08 M_{\odot}$ being the minimum mass for a star, the object acting as a lens could be either a brown dwarf or a low-mass star. This is another demonstration of the extreme “sensitivity” of the gravitational microlensing technique to catch effects caused by very light objects. Consequently, gravitational microlensing also permits the detection of these kinds of objects, which, otherwise, are impossible to detect in faraway galaxies.

Author Contributions: Conceptualization, M.C., F.D.P., A.F. and A.N.; methodology, F.D.P. and A.N.; software, M.C. and A.F.; validation, M.C., A.F. and A.N.; formal analysis, M.C. and A.F.; data curation, M.C. and A.F.; writing—original draft, M.C.; writing—review and editing, F.D.P., A.F. and A.N.; visualization, A.F. and A.N.; supervision, F.D.P. and A.F. All authors have read and agreed to the published version of the manuscript.

Funding: This research received no external funding.

Institutional Review Board Statement: Not applicable.

Data Availability Statement: The original data presented in the study are openly available in “ZTF Public Data Releases” at <https://www.ztf.caltech.edu/ztf-public-releases.html> (accessed on 7 September 2025).

Acknowledgments: TAsP (Theoretical Astroparticle Physics) and Euclid INFN Scientific Projects are acknowledged. The two anonymous reviewers are also acknowledged for their comments.

Conflicts of Interest: The authors declare no conflicts of interest.

Abbreviations

The following abbreviations are used in this manuscript:

AGN	Active Galactic Nucleus
GW	Gravitational Wave
ZTF	Zwicky Transient Facility
BBH	Binary Black Hole
PSPL	Point Source Point Lens
LM	Levenberg–Marquardt
DE	Differential Evolution
MCMC	Markov Chain Monte Carlo
FSPL	Finite Source Point Lens
USBL	Uniform Source Binary Lens
AU	Astronomical Unit
MJD	Modified Julian Date
SMBH	Supermassive Black Hole

Note

- 1 The ZTF is a time-domain optical survey performed by the Palomar 48-inch (1.22 m) Schmidt Telescope. Its camera is characterized by 16 CCDs of 6144×6160 pixels each, providing an area of 47 deg^2 for every exposure. The telescope operates with a limiting magnitude of 20.8 in the *g* band and 20.6 in the *r* band (for further details see [5]).
- 2 In this work, we have used the version number 1.9.7 of pyLIMA.

References

1. Aasi, J. et al. [The LIGO Scientific Collaboration]. Advanced LIGO. *Class. Quantum Grav.* **2015**, *32*, 074001.
2. Acernese, F.; Agathos, M.; Agatsuma, K.; Aisa, D.; Allemandou, N.; Allocata, A.; Amarni, J.; Astone, P.; Balestri, G.; Ballardin, G. et al. Advanced Virgo: A second-generation interferometric gravitational wave detector. *Class. Quantum Grav.* **2015**, *32*, 024001.
3. Graham, M.J.; Ford, K.E.S.; McKernan, B.; Ross, N.P.; Stern, D.; Burdge, K.; Coughlin, M.; Djorgovski, S.G.; Drake, A.J.; Duev, D.; et al. Candidate Electromagnetic Counterpart to the Binary Black Hole Merger Gravitational-Wave Event S190521g. *Phys. Rev. Lett.* **2020**, *124*, 251102.

4. Abbott, R.; Abbott, T.D.; Abraham, S.; Acernese, F.; Ackley, K.; Adams, C.; Adhikari, R.X.; Adya, V.B.; Affeldt, C.; Agathos, M. et al. GW190521: A Binary Black Hole Merger with a Total Mass of $150 M_{\odot}$. *Phys. Rev. Lett.* **2020**, *125*, 101102.
5. Bellm, E.C.; Kulkarni, S.R.; Graham, M.J.; Dekany, R.; Smith, R.M.; Riddle, R.; Masci, F.J.; Helou, G.; Prince, T.A.; Adams, S.M.; et al. The Zwicky Transient Facility: System Overview, Performance, and First Results. *Publ. Astron. Soc. Pac.* **2018**, *131*, 018002.
6. Morton, S.L.; Rinaldi, S.; Torres-Orjuela, A.; Derdzinski, A.; Vaccaro, M.P.; Del Pozzo, W. GW190521: A binary black hole merger inside an active galactic nucleus? *Phys. Rev. D.* **2023**, *108*, 123039.
7. De Paolis, F.; Nucita, A.A.; Strafella, F.; Licchelli, D.; Ingrosso, G. A quasar microlensing event towards J1249+3449? *Mon. Not. R. Astron. Soc.* **2020**, *499*, L87–L90.
8. Bachelet, E.; Norbury, M.; Bozza, V.; Street, R. pyLIMA: An Open-source Package for Microlensing Modeling. I. Presentation of the Software and Analysis of Single-lens Models. *Astron. J.* **2017**, *154*, 203.
9. Gould, A. A Natural Formalism for Microlensing. *Astrophys. J.* **2000**, *542*, 785.
10. Fluke, C.J.; Webster, R.L. Investigating the geometry of quasars with microlensing. *Mon. Not. R. Astron. Soc.* **1999**, *302*, 68–74.
11. Paczyński, B. Gravitational Microlensing by the Galactic Halo. *Astrophys. J.* **1986**, *304*, 1–5.
12. Lee, C.-H.; Riffeser, A.; Seitz, S.; Bender, R. Finite-Source Effects in Microlensing: A Precise, Easy to Implement, Fast, and Numerically Stable Formalism. *Astrophys. J.* **2009**, *695*, 200–207.
13. Tsapras, Y. Microlensing Searches for Exoplanets. *Geosciences* **2018**, *8*, 365.
14. Einstein, A. Lens-Like Action of a Star by the Deviation of Light in the Gravitational Field. *Science* **1936**, *84*, 506–507.
15. Paczyński, B. Gravitational Microlensing in the Local Group. *Annu. Rev. Astron. Astrophys.* **1996**, *34*, 419–460.
16. Witt, H.J. Investigation of high amplification events in light curves of gravitationally lensed quasars. *Astron. Astrophys.* **1990**, *236*, 311–322.
17. Witt, H.J.; Mao, S. Can Lensed Stars Be Regarded as Pointlike for Microlensing by MACHOs? *Astrophys. J.* **1994**, *430*, 505–510.
18. Nucita, A.A.; Licchelli, D.; De Paolis, F.; Ingrosso, G.; Strafella, F.; Katysheva, N.; Shugarov, S. Discovery of a bright microlensing event with planetary features towards the Taurus region: A super-Earth planet. *Mon. Not. R. Astron. Soc.* **2018**, *476*, 2962–2967.
19. Giordano, M.; Nucita, A.A.; De Paolis, F.; Ingrosso, G. Timing analysis in microlensing. *Int. J. Mod. Phys. D* **2017**, *26*, 1741009.
20. Nucita, A.A.; Giordano, M.; De Paolis, F.; Ingrosso, G. Signatures of rotating binaries in microlensing experiments. *Mon. Not. R. Astron. Soc.* **2014**, *438*, 2466–2473.

Disclaimer/Publisher’s Note: The statements, opinions and data contained in all publications are solely those of the individual author(s) and contributor(s) and not of MDPI and/or the editor(s). MDPI and/or the editor(s) disclaim responsibility for any injury to people or property resulting from any ideas, methods, instructions or products referred to in the content.